2026 IEEE International Conference on Robotics and Automation (ICRA 2026)
June 1-5, 2026. Vienna, Austria

A Novel Dual-Spherical Intelligent Pipeline Robot for Leak Detection

Zefeng Yan[1,2], Lei Wei[1], Liang Lu[1], Zhou Yang[1], Jiacheng Wang[1], and Bin Han[1,*],Senior Member, IEEE

***Abstract*— To address the challenge of achieving both low drag and high maneuverability in complex water-filled pipeline environments, this study proposes a novel dual-spherical pipeline robot with integrated leak detection and mapping capabilities. A multi-objective optimization framework was established to simultaneously improve hydrodynamic performance, motion stability, and internal spatial layout, while adopting a streamlined shell design to achieve both low-drag and sensor integration requirements. Based on a task-driven configuration optimization method, an energy-efficient propeller arrangement was derived under the constraint of maintaining maneuvering performance. The robot employs a helical differential propulsion system and integrates multiple sensors, including a vision module, an inertial navigation unit, and a pressure sensor, to enable leak detection and mapping. Its fully sealed spherical housing ensures stable operation in water-filled pipelines. Based on the proposed configuration, an experimental platform incorporating four representative pipeline environments was constructed, and a series of inspection, mapping, and environmental adaptability tests were conducted. The results demonstrate that the robot can achieve agile turning and stable locomotion in water-filled pipelines, showing strong potential for practical engineering applications.**

***Index Terms*- Mechanical design, multi-objective optimization, leak detection, pipeline robot.**

I. INTRODUCTION

Pipelines are essential infrastructure for transporting oil, natural gas, and domestic water, offering high efficiency, low cost, and environmental benefits, and are therefore widely used. However, long-term operation in complex environments makes them susceptible to aging-related issues such as corrosion, fatigue cracking, and plastic deformation, which can lead to resource loss and environmental contamination [1], [2], [3], [4]. Ensuring their safe operation thus requires addressing both traditional risks and emerging challenges [5]. To ensure transport safety while controlling maintenance costs, pipelines must undergo regular inspection and servicing. However, they are often buried underground or laid underwater, and they vary in diameter and structural configuration, making condition assessment, leakage detection, and fluid quality monitoring technically challenging [6]. Conventional manual inspection methods are inefficient, inaccurate, and hazardous [7]. The development of multifunctional pipeline robots can help reduce maintenance costs and time while providing a more efficient and reliable solution for pipeline inspection and maintenance.

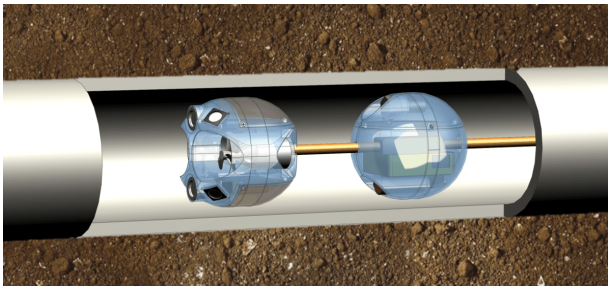

Fig. 1: Fully waterproof dual-spherical pipeline inspection robot

Research on pipeline robots has advanced considerably, with their driving mechanisms and structural configurations becoming increasingly diverse. Based on their propulsion methods, they can be broadly classified into unpowered pipeline inspectors, wheeled, tracked, screw-driven, and bio-inspired types.

Pipeline inspectors propelled by the internal fluid pressure rely on the natural flow within the pipeline. These robots [8], [9]have simple structures and can travel smoothly through straight sections to perform inspection tasks. However, their applicability in complex geometries such as bends is limited, as their motion trajectory and speed are difficult to control precisely due to their dependence on the fluid flow. Wheeled pipeline robots achieve locomotion by installing drive wheels on the bottom or around the circumference of the body, offering advantages such as high versatility, low cost, and simple control. T. Oka et al. [10] developed the AIRo series of robots featuring multi-segment and multi-active-wheel designs. To further enhance adaptability in complex pipeline environments, the improved model AIRo-3.1 adopted a more compact multi-link joint-wheel structure. To address the challenge of navigating confined pipelines such as small-curvature C-shaped and T-junction pipes, S. Kakogawa et al. [11] proposed an automatic T-branch traversal method for the jointed-wheeled robot AIRo-5.2, which uses joint-angle responses to environmental changes for navigation. R. Elankavi et al. [12] compared robots equipped with planar joints and telescopic joints, and found that when overcoming long obstacles, an independent joint mechanism helps keep the wheels continuously in contact with the pipe wall.Nevertheless, wheeled robots have difficulty passing through diameter transitions, C-shaped pipes, and

*Corresponding author: Bin Han (binhan@hust.edu.cn).
[1]State Key Laboratory of Intelligent Manufacturing Equipment and Technology, School of Mechanical Science and Engineering, Huazhong University of Science and Technology, Wuhan, China.
[2]School of Automation and Software Engineering, Shanxi University, Taiyuan, China.
This work was partially supported by the National Natural Science Foundation of China under Grant No. 52375015, in part by the Jing-Jin-Ji Regional Integrated Environmental Improvement National Science and Technology Major Project under Grant No. 2025ZD1206400, and in part by the Interdisciplinary Research Program(Robotics and Artificial Intelligence) of HUST under Grant2024JCYJ037.

T-junctions, and often suffer from insufficient traction that can lead to slippage. Tracked pipeline robots significantly enhance traction through their track structures and can adapt to different pipe diameters by adjusting the track inclination angles. Such robots offer several advantages, including high traction, flexible maneuverability, strong anti-slip performance, and robust obstacle crossing capability. Y. Kwon et al. [13] developed a dual-ball cooperative robot for indoor pipeline inspection, which employs differential drive and a spring-loaded four-bar mechanism to allow the robot to expand and closely adhere to the pipe wall. Considering the geometric constraints imposed by the pipe walls during locomotion, Z. Zheng et al. [14] investigated the key parameter design of a wall-pressing tracked pipeline robot under multiple constraints, and proposed an optimization method for its length, width, and head-waist joint angles to improve traversal performance in C-shaped and T-junction pipes. Nevertheless, tracked robots also suffer from certain drawbacks, such as relatively large weight and bulk, and limited steering flexibility, which makes turning or reversing especially challenging in confined spaces. Helical-drive pipeline robots achieve locomotion by rotating in a helical pattern along the pipe wall. X. Yin et al.[15] proposed an adaptive variable-pitch helical pipeline robot capable of smoothly traversing vertical pipelines with diameters of 160 mm and curvature angles up to 90°. L. Wang et al. [16] developed an electric helical-wheeled robot designed for multi-diameter pipelines and steep inclines. This robot demonstrated stable operation in pipes with diameters ranging from 110 to 180 mm, and exhibited excellent climbing and expansion capabilities.Constrained by the limited adaptability of rigid structures to complex and variable pipeline environments, researchers have explored bionic designs to enhance robotic performance. For example, Li et al.[17] developed a soft pipeline robot inspired by inchworms, while Liu et al. [18] proposed a helical gait for snake-like robots designed for inner-wall inspection. Xie et al.[19] employed a bioinspired robotic fish for pipeline inspection, and Oyama et al. [20] utilized a worm-like robot to generate three-dimensional maps of pipeline interiors.

To enable stable locomotion of pipeline robots within pipeline systems, two primary challenges must be addressed. First, the robot must operate stably in water-filled pipelines and maintain efficient propulsion against hydrodynamic resistance. Second, it must exhibit high turning agility under water-filled conditions to achieve flexible maneuverability.

To tackle these challenges, this study introduces a pipeline robot with a novel dual-spherical configuration (shown in Fig. 1) and makes two main contributions.1) A multi-objective optimization framework was established to jointly optimize hydrodynamic performance, motion stability, and internal spatial layout. The robot's outer shell was designed with a streamlined shape and a fully sealed structure, allowing it to operate reliably in water-filled pipelines. 2) A capability boundary based configuration optimization was conducted. By minimizing system energy consumption while ensuring maneuvering performance, the optimal configuration of the propellers was derived, based on which a helical differential propulsion mechanism was designed. Furthermore, multiple onboard sensors, including a vision module, an inertial navigation unit, and a pressure sensor, were integrated into the system. This novel pipeline robot not only retains the maneuverability of existing designs but also achieves higher locomotion speed and full waterproof capability.

II. Optimal Layout Design for Pipeline Robots

To achieve efficient hydrodynamic performance for the pipeline robot, it is essential to precisely design the dimensional parameters and spatial arrangement of its components. The optimization process is based on a multi-objective optimization framework[23], as shown in Fig. 2. This framework enables a systematic analysis and improvement of the robot's design. For the same cross-sectional area, a spherical configuration can significantly reduce overall drag. Therefore, a spherical outer shell was adopted in this study. Within the multi-objective optimization approach, we considered not only hydrodynamic performance but also the robot's stability and internal spatial requirements for its components. By adjusting the spatial positions of each component, the optimal design solution was determined. A cross-sectional view of the spherical structure is shown in Fig. 3.

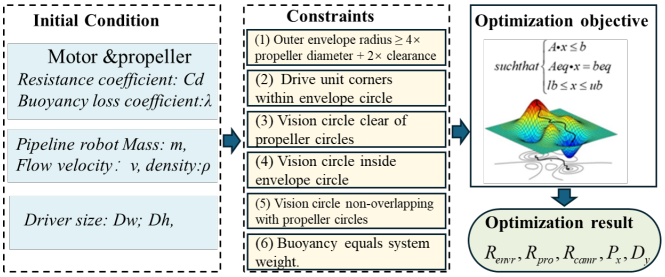

Fig. 2: Multi-objective optimization framework

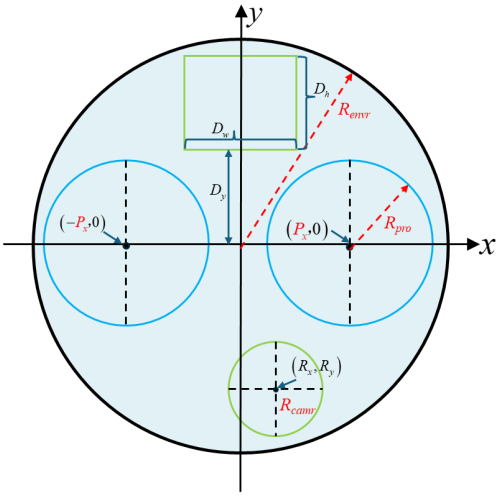

Fig. 3: Cross-sectional parameters of the pipe robot

- Optimization variables
- R_{envr}: radius of the outer envelope
- R_{pro}: radius of the thruster
- R_{camr}: radius of the camera mount
- P_x: distance from the thruster to the center of the sphere
- D_y: radial distance from the drive module to the center of the sphere
- (R_x, R_y): distance from the vision module center to the center of the sphere

The optimization objective function of the layout configuration of the pipeline robot is expressed as:

$$\min J = \begin{bmatrix} f_1(R_{envr}) & -R_{pro} & -R_{camr} & -P_x & f_2(R_{envr}, R_{pro}) \end{bmatrix} \tag{1}$$

where, $f_2(R_{envr}, R_{pro}) = \left[4/3\pi {R^3}_{envr} - 4\lambda\pi R_{pro} \cdot 2R_{envr}\right]\rho - m$, $f_1(R_{envr}) = 1/2 C_d(\pi {R^2}_{envr})v^2$, ρ denotes the fluid density, m represents the total mass, λ is the buoyancy loss coefficient accounting for geometric corrections caused by irregular shapes, C_d is the drag coefficient, and v is the relative velocity.

In Equation (1), the first objective is to minimize the overall hydrodynamic drag, thereby improving energy efficiency. Second, the optimization seeks to enlarge the spatial radius available for propeller installation, aiming to generate stronger thrust and enhance propulsion capability. Third, we aim to maximize the spatial radius for mounting cameras and other sensors, allowing for a greater number of sensors to be integrated, thus improving monitoring and perception capacity. Fourth, positioning the thrusters as far as possible from the sphere's center is another key objective, as this configuration produces larger yaw moments and improves maneuverability. Finally, the optimization ensures that buoyancy and gravity are balanced during level navigation, thereby avoiding additional energy consumption for buoyancy control and enhancing overall energy utilization efficiency.

The mathematical form of the constraint condition is:

$$\begin{cases} 4R_{pro} + 2P_x \le R_{envr} \\ (D_y + D_h)^2 + \left(D_w/2\right)^2 \le R^2_{envr} \\ (R_x - P_x)^2 + (R_y)^2 \ge (R_{pro} + R_{camr})^2 \\ (R_x)^2 + (R_y)^2 \le (R_{envr} - R_{camr})^2 \\ (P_x - D_w/2)^2 + D^2{}_y \ge R^2{}_{pro} \\ \left[\frac{4}{3}\pi {R^3}_{envr} - 4\lambda\pi R_{pro} \cdot 2R_{envr}\right]\rho - m \ge 0 \end{cases} \tag{2}$$

Constraints: 1) The minimum outer envelope radius must exceed four times the propeller diameter plus twice the mounting clearance. 2) The four corner points of the drive unit must lie within the outer envelope circle. 3) The vision module mounting circle must not interfere with the propeller mounting circles. 4) The vision module mounting circle must be located within the outer envelope circle. 5) The vision module mounting circle must not overlap with the propeller mounting circles. 6) Buoyancy must balance the system weight.

The value range of each optimization variable is: $R_{envr} \in [0, 100]$, $R_{pro} \in [0, 90]$, $R_{camr} \in [0, 80]$, $P_x \in [0, 50]$,$D_y \in [0, 50]$, $R_x \in [-50, 50]$, $R_y \in [-50, 0]$. The known parameter values are as follows: $D_w = 25mm$, $D_h = 20mm$, $C_d = 1$, $v = 1m/s$, $\rho = 998.9$, $m = 0.5kg$, $\lambda = 2/3$. For this optimization problem, multiple objectives are involved, and thus a Pareto solution set is required. Each objective is normalized, and the solution closest to the origin in the normalized objective space is selected as the final compromise solution. Specifically, Fig. 4 illustrates the Pareto solution set for objectives 1, 2, and 3, where the red point represents the final compromise solution. This solution satisfies the following conditions: the outer envelope radius is minimized to reduce overall drag, meanwhile, the spatial radius for thruster installation is maximized, and the spatial radius for sensor installation is also maximized, thereby accommodating electronic components such as vision cameras. This approach ensures the identification of a balanced trade-off among multiple objectives, leading to an overall optimal performance.

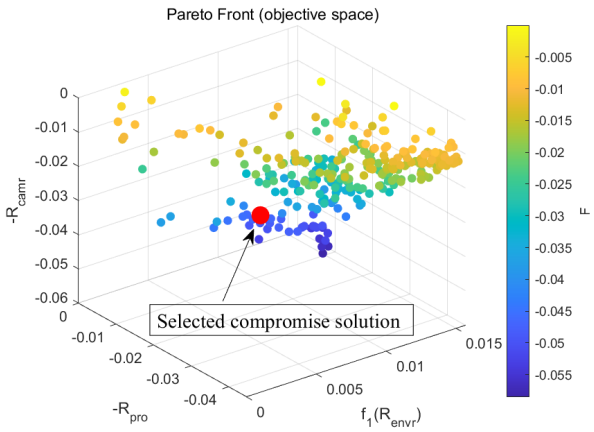

Fig. 4: Optimize the Pareto solution set of the variable (the red point indicates the final compromise solution)

The values of each optimization variable corresponding to the optimal compromise solution are: $R_{envr} = 84.9$ mm, $R_{pro} = 20.0$ mm, $R_{camr} = 9.5$ mm, P_x = 12.7 mm, $D_y = 20.5$ mm,$R_x = -13.1$ mm,$R_y = -26.6$ mm.

III. Collaborative Optimization of Thruster Configuration Based on Task

A. Motion planning for pipeline inspection robots

To align with the predetermined operational scenario, a common trajectory tracking task for a pipeline robot equipped with survey instruments is pipeline scanning as shown in Fig. 5. In this task, the pipeline robot encounters several straight lines and sharp turns. The desired trajectory for the pipeline scan is defined as:

$$\eta_d(t) = \begin{cases} [0, 0, f_1(t, k_1), 0, 0, 0] & 0\,\text{s} \le t \le 9\,\text{s}, \\ [f_1(t-9, -k_2), 0, z_1, 0, 0, 0] & 9\,\text{s} \le t \le 18\,\text{s}, \\ [x_1, 0, z_1, 0, 0, f_3(t-18, k_3)] & 18\,\text{s} \le t \le 24\,\text{s}, \\ [x_1, f_2(t-24, k_2), z_1, 0, 0, \pi/2] & 24\,\text{s} \le t \le 33\,\text{s}, \\ [x_1, y_1, z_1, 0, 0, \pi/2 - f_3(t-33, k_3)] & 33\,\text{s} \le t \le 39\,\text{s}, \\ [x_1 + f_2(t-39, k_2), y_1, z_1, 0, 0, 0] & 39\,\text{s} \le t \le 48\,\text{s}, \\ [x_1 + f_2(9, k_2), y_1, z_1, 0, 0, 0] & 48\,\text{s} \le t \le 57\,\text{s}. \end{cases} \tag{3}$$

Where $f_1(t,k), f_2(t,k)$ represents the processes of acceleration, constant speed, and deceleration during each segment of motion, as shown in the following equation:

$$f_1(t,k)=\begin{cases}6k/\pi(-1+\cos(\pi t/6) & 0\,\mathrm{s}\le t\le 3\,\mathrm{s},\\ k(-6/\pi-t+3) & 3\,\mathrm{s}\le t\le 6\,\mathrm{s},\\ 6k/\pi(-1+\cos(\pi(t-3)/6))-3k & 6\,\mathrm{s}\le t\le 9\,\mathrm{s}.\end{cases} \tag{4}$$

$$f_2(t,k)=\begin{cases}6k/\pi(1-\cos(\pi t/6)) & 0\,\mathrm{s}\le t\le 3\,\mathrm{s},\\ k(6/\pi+t-3) & 3\,\mathrm{s}\le t\le 6\,\mathrm{s},\\ 6k/\pi(1-\cos(\pi(t-3)/6))+3k & 6\,\mathrm{s}\le t\le 9\,\mathrm{s}.\end{cases} \tag{5}$$

$$f_3(t,k)=\begin{cases}4k/\pi(1-\cos(\pi t/4)) & 0\,\mathrm{s}\le t\le 2\,\mathrm{s},\\ k(4/\pi+t-2) & 2\,\mathrm{s}\le t\le 4\,\mathrm{s},\\ 4k/\pi(1-\cos(\pi(t-2)/4))+2k & 4\,\mathrm{s}\le t\le 6\,\mathrm{s}.\end{cases} \tag{6}$$

$k_1=0.6, k_2=1.5, k_3=0.3455$ respectively represent the velocities during the constant speed segments in the underwater robot sinking, forward, and turning motions. $x_1=y_1=f_2(9,k_1), z_1=f_1(9,k_2)$ represents the state of the pipeline robot at the end of a motion segment.

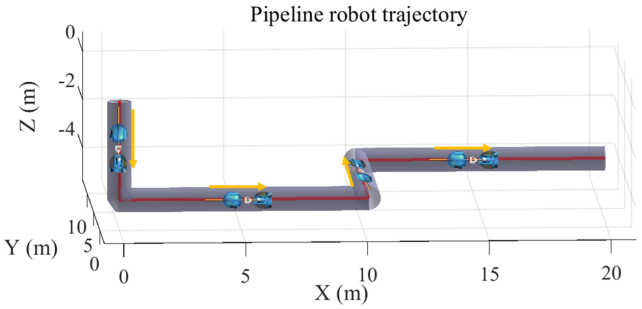

Fig. 5: The trajectory of the pipeline robot's detection task

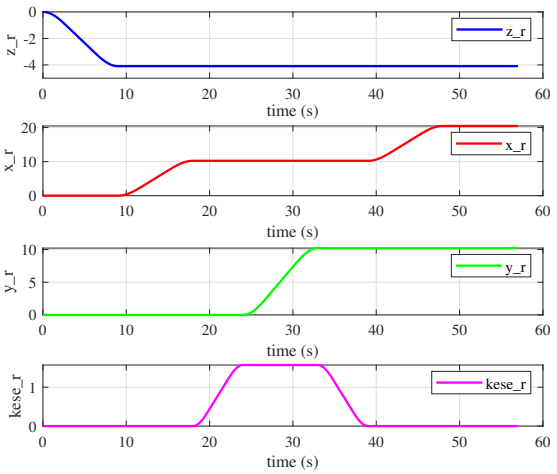

Fig. 6: The trajectories of each degree of freedom in the robot inspection task

B. Optimization of thruster configuration considering system energy consumption

When the expected trajectory is obtained, the linear and angular velocity vectors in the machine coordinate system can be derived through coordinate transformation:

$$v=J^{-1}(\eta)\,\dot{\eta} \tag{7}$$

where $\eta=[x,y,z,\varphi,\theta,\psi]^T$ is a vector contains the position and Euler angles of the robot in the inertial frame, $v=[u,v,w,p,q,r]^T$ is a vector of linear and angular velocities in the body-fixed frame, and $J(\eta)$ is the transformation matrix relating to the two frames.

When external disturbances are neglected, the required forces or moments for achieving a desired trajectory can be precisely calculated by constructing a general underwater dynamic model. The six degrees of freedom (6-DOF) underwater dynamic equations are expressed as:

$$\mathbf{M}v+\mathbf{C}(v)v+\mathbf{D}(v)v+\mathbf{g}(\eta)=\tau \tag{8}$$

where, $\mathbf{M}$ denotes the sum of the inertia matrix and the added mass matrix, $\mathbf{C}(v)$ represents the coriolis and centrifugal matrix, $\mathbf{D}(v)$ is the viscous hydrodynamic damping matrix of the pipeline robot, and $\mathbf{g}(\eta)$ corresponds to the restoring force matrix arising from the robot's weight and buoyancy. The control input τ is determined from the thrust vector f and the configuration matrix $\mathbf{B}$, and is expressed as:

$$\tau=\mathbf{B}\mathbf{f} \tag{9}$$

where, $\mathbf{f}=\begin{bmatrix}T_1 & T_2 & \dots & T_m\end{bmatrix}^T$ and T_i denotes the output thrust of the i-th thruster. The configuration matrix is determined by the position vectors and thrust directions of the thrusters. The force and moment vector generated by the i-th thruster acting on the robot can be expressed as:

$$B_i=\begin{bmatrix}r_i\\ d_i\times r_i\end{bmatrix} \tag{10}$$

where, $\mathbf{B}=\begin{bmatrix}B_i & B_2 & \dots & B_m\end{bmatrix}$.

From equations (8)-(10) above, the variables that influence the resultant force and moment of the system include the orientation and position vectors of the thrusters. These variables jointly determine the spatial arrangement and effectiveness of the thrusters. Each individual thruster has six degrees of freedom (DOFs) in space, corresponding to three translational and three rotational components. In this study, we do not consider positional variations of the thrusters but instead focus on optimizing their orientations. Consequently, the number of optimization variables for each thruster is reduced to two angular parameters, θ and α. These two angles define the spatial orientation of the thruster and play a critical role in the distribution of the system's resultant force and moment. Taking spatial constraints and optimization efficiency into account, the number of thrusters is set to two. The spatial positions and orientations of these two thrusters must be carefully designed to achieve optimal system performance. Their corresponding thruster orientation matrices

can be expressed as $r_i = [\sin\theta\cos\alpha, \sin\theta\sin\alpha, \cos\theta]^T$. By appropriately selecting and optimizing the orientation angles θ and α of the two thrusters, the system's resultant force and moment can be effectively controlled, thereby enabling precise regulation of its motion state.

The objective of the optimization is to determine the propeller configuration that minimizes energy consumption while meeting the required velocity, acceleration, and force/moment specifications. By optimally combining the parameters of each component within the propulsion system, energy consumption can be significantly reduced and overall efficiency improved, without compromising performance criteria. The following optimization problem is defined: minimize with respect to the following criterion:

$$J(\alpha,\theta,u,s) = \sum_{i=1}^{m} W_i(u_i) + s^T Q s + (\alpha-\alpha_0)^T \Omega (\alpha-\alpha_0) + (\theta-\theta_0)^T \Gamma (\theta-\theta_0) + \frac{\rho}{\varepsilon + \det\left(B(\alpha,\theta)B^T(\alpha,\theta)\right)} \tag{11}$$

$$s = \tau - B(\alpha,\theta)u \tag{12}$$

$$u_{\min} \le u \le u_{\max}. \tag{13}$$

$$\alpha_{\min} \le \alpha \le \alpha_{\max} \tag{14}$$

$$\theta_{\min} \le \theta \le \theta_{\max} \tag{15}$$

$$\Delta\alpha_{\min} \le \alpha - \alpha_0 \le \Delta\alpha_{\max} \tag{16}$$

$$\Delta\theta_{\min} \le \theta - \theta_0 \le \Delta\theta_{\max} \tag{17}$$

The power consumption term is reflected in the first component of the objective function, which accounts for the power consumed by each actuator, denoted as $W_i(u_i)$, it is defined as $W_i(u_i) = k_i|u_i|^{3/2}$. The second term $s^T Q s$ represents the deviation between the predicted and actual forces and moments generated by the pipeline robot in response to the desired trajectory, as specified in constraint (12). The weighting matrix Q must be set with sufficiently large eigenvalues to ensure that constraint (13), which bounds the maximum and minimum forces and moments generated by the thrusters, U_{min} is U_{max} satisfied. and denote the lower and upper limits of thrust, respectively. Constraints (14) and (15) specify the lower and upper bounds of the thruster deflection angle, namely $\alpha_{\min}$,$\alpha_{\max}$ and $\theta_{\min}$, $\theta_{\max}$. Constraints (16) and (17) impose limits on the rate of change of the control inputs, ensuring that only moderate variations are permitted between successive time steps. The weighting matrix $\Omega > 0$ is introduced to balance the relative importance of these objectives, while α_0 and θ_0 denote the orientation angles at the previous time step. Singularities are avoided through the fifth term in the criterion, where $\varepsilon > 0$ is imposed to prevent numerical issues, ρ serves as a weighting parameter.

The optimization problem can be solved by reformulating it as a sequential quadratic programming (SQP) problem. In this study, the maximum forward and reverse thrust of each thruster is set to 5 N. The angle ranges are defined as $\theta \in [0, \pi/2]$ and $\alpha \in [0, \pi]$. The weighting matrices are specified as $Q = diag[10,10]$, $\Omega = diag[1,1]$, and $\Gamma = diag[1,1]$, with $\varepsilon = 1$. Fig. 7 presents a comparison between the desired force and the actual force output of the optimized configuration. The ref curve represents the theoretical force required for the pipeline robot to follow the prescribed trajectory, while the actual curve reflects the forces generated by the thrusters. It can be seen that the optimized configuration enables the actual output forces to fully meet the expected targets while simultaneously minimizing energy consumption. This result demonstrates that, after optimization, the system not only achieves excellent force-tracking performance but also attains an ideal energy efficiency ratio, highlighting the effectiveness of the optimized design.

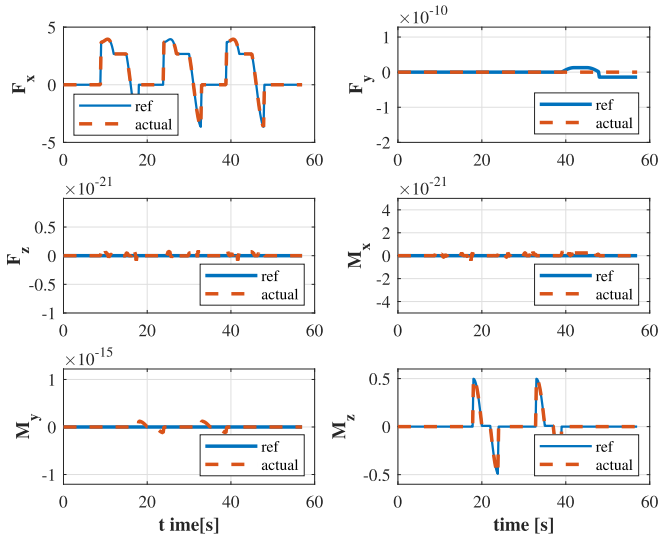

Fig. 7: Optimization configuration performance verification: Expected forces and actual generated forces in each direction under the machine coordinate system

Fig. 8 (a) illustrates the optimized configuration, where $\theta = \pi/2$ and $\alpha = 0$. Fig. 8 (b) compares the actual capability boundary of the configuration with the required one, clearly showing their distribution and degree of alignment. The red boundary represents the capability required to accomplish the prescribed trajectory, while the colored region indicates the maximum capability achievable by the system. This relationship indicates that the actual capability boundary of the optimized configuration not only fully encompasses the required boundary but also provides a certain degree of redundancy. This redundancy provides sufficient assurance for stable operation and handling unexpected situations, thereby enhancing the system's reliability and adaptability in diverse and complex environments and tasks. A dual-sphere robot prototype was designed based on the optimization results, as shown in Fig. 9. Its key dimensions were determined based on the previous optimization results.

C. Hydrodynamic performance evaluation

Fig. 10 (a) shows the velocity field distribution of the dual-sphere pipeline robot in an underwater environment. The surrounding fluid exhibits a clear velocity gradient, with smooth streamlines at the front and no noticeable flow blockage or large-scale separation at the rear, indicating

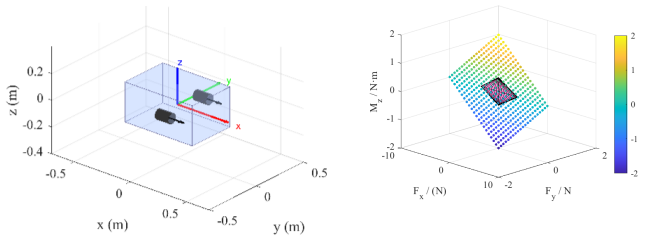

(a) (b)

Fig. 8: (a) Optimized dual-propeller layout, $\theta = \pi/2$ and $\alpha = 0$, (b) The comparison between the required capability boundary and the capability boundary generated by the actual configuration.

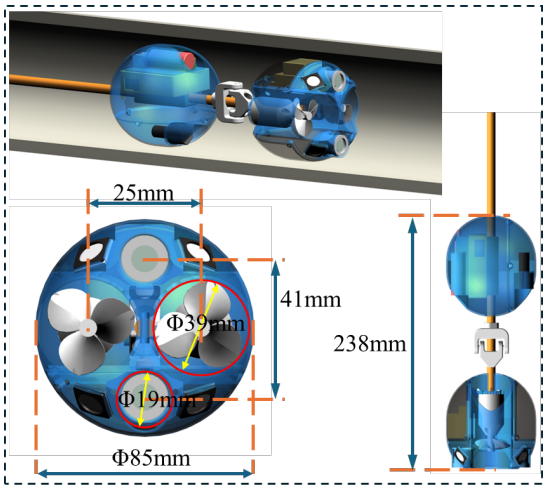

Fig. 9: Three-view of the dual-ball pipeline robot

favorable hydrodynamic performance. Fig. 10 (b) shows the turbulence field, where higher turbulence intensity occurs near the connection region and in the wake, yet remains within a reasonable range without forming strongly unstable vortex structures. As shown by the streamlines in Fig. 10 (c), local recirculation zones and vortices form around the front sphere, helping to reduce pressure drag. Simulation results show that at a flow velocity of 0.5 m/s, the robot experiences a drag force of 0.499 N, corresponding to a drag coefficient C_D=0.58, confirming the effectiveness of its low-drag design.

IV. Experiment

A. Pipeline robot

Fig. 11 shows the hardware and software architecture of the integrated pipeline robot. The hardware subsystem consists of a controller, an inertial navigation system (INS), stereo and monocular cameras, a lithium-ion battery, a hydrophone, a pressure sensor, thrusters, and an underwater light. The controller fuses sensor data and commands actuators, while the stereo and monocular cameras provide 3D perception and visual coverage. The battery powers the system, the hydrophone enables underwater communication,

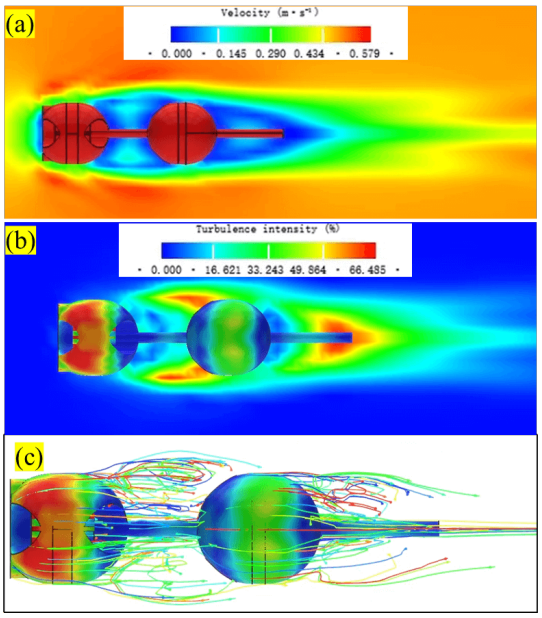

Fig. 10: (a) Velocity field, (b) turbulence field distribution, (c) fluid trace

the pressure sensor measures depth, the thrusters generate propulsion, and the light provides illumination. The software is integrated into a handheld terminal equipped with a high-definition display and control interface, enabling real-time environmental visualization, button-based control of motion and functions, and data logging. By tightly coupling hardware and algorithms, the robot can autonomously perform inspection tasks in complex pipeline environments.

B. Experiments and results

To comprehensively evaluate the turning maneuverability and water-tightness of the pipeline robot developed in this study, we conducted a series of detailed experiments. Fig. 12(a) presents an image sequence, panels (a)-(d), depicting the process from start-up to completion of a turn. The frames show that the robot can execute an approximately 180° turn, demonstrating excellent maneuverability.The robot?s waterproof rating was validated through a 24-hour immersion test. During the test, the device was fully submerged at a depth of 0.5 meters, and its internal electronic compartments remained completely dry, confirming the integrity of its sealing. We further assessed performance in a T-shaped pipeline. Fig. 12(b) records the robot's motion within the T-junction. In this experiment, the pipe was placed in a water tank and fully flooded prior to testing. The sequence in panels (a)-(d) shows that the robot traversed the vertical branch of the T-junction smoothly, confirming not only strong turning capability but also adaptability and reliability in complex pipeline environments. These results highlight the robot's substantial potential for practical deployment. Fig. 13(a) shows tests in a fully water-filled pipeline environment with diameters ranging from 100 to 400 mm. The experimental pipeline setup included 100 mm-diameter transparent plastic pipes, 100 mm diameter metal pipes, as well as 200 mm diameter

Fig. 11: Hardware and software system of pipeline robots

plastic and metal pipes. In addition, the system incorporated various structural elements such as elbow sections and T-junctions. Fig. 13(b) shows the robot operating inside a metal pipeline, together with the internal environment visualized through the graphical user interface. Fig. 13(c) presents the robot navigating within a plastic water-supply pipeline and transmitting real-time visual information. A communication cable is connected to the rear of the robot. Control commands are issued from the PC-based GUI, transmitted wirelessly to a spooler device, and then delivered to the robot body via a waterproof Ethernet cable.

The robot is equipped with an inertial navigation module comprising a dual-axis accelerometer and a gyroscope: the accelerometer estimates the pose of the robot relative to the global coordinate frame during pipeline locomotion, while the gyroscope measures the rotation angle as the robot passes through curved sections. In addition, a micro-camera mounted on the robot enables visual inspection of the pipeline interior, with the images displayed in real time through the GUI. Experimental results demonstrate that the maximum traveling speed of the robot reaches 50 cm/s.

As shown in Table I, the pipeline robot developed in this study outperforms existing robots in several key aspects. The pip-diameter range indicates the range of pipe diameters that the robot can adapt to. While most existing robots are designed for either relatively narrow or wide single pipe ranges (e.g., Kako [8]; Li [19]), our robot covers a much broader range of 100-400 mm, greatly enhancing

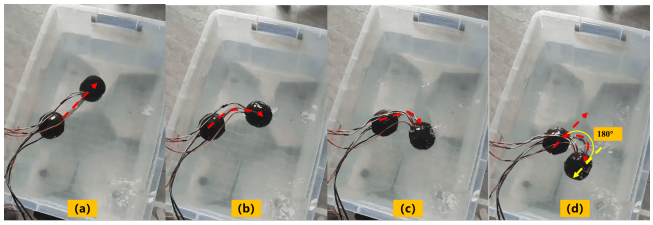

(a) Turning performance and water tightness tests in a water tank

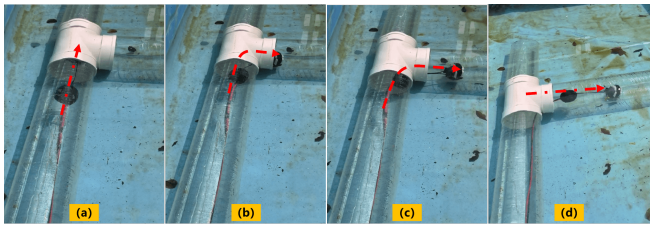

(b) Turning capability test in a T-junction pipeline

Fig. 12: Waterproofing and turning capability tests.

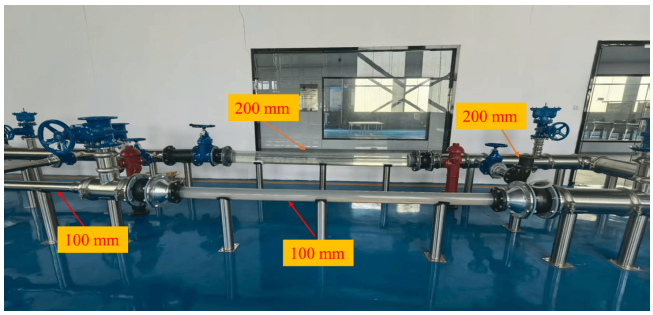

(a) Pipeline testing platform

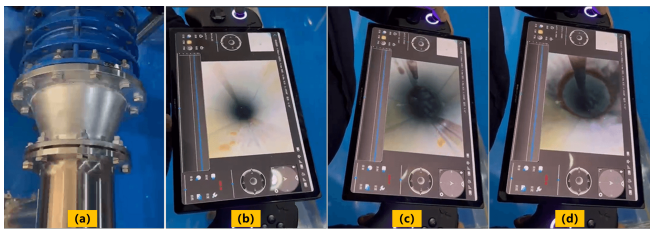

(b) Performance testing in metal pipes (diameter 100 mm)

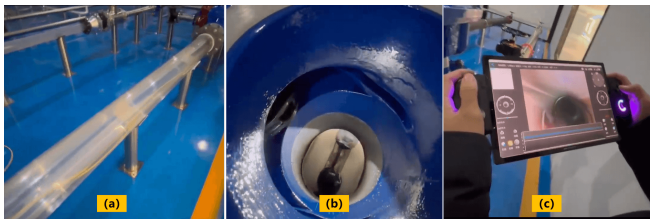

(c) Motion test in plastic pipes (diameter 100 mm)

Fig. 13: Testing process in water supply pipelines.

adaptability. In terms of mobility, it reaches a speed of 50.0 cm/s, while weighing only 1.0 kg. Moreover, it is the only robot in the table with full waterproof capability, enabling stable operation in water-filled pipelines and overcoming the common lack of sealing and waterproofing in existing designs.

TABLE I: COMPARISON OF THE DEVELOPED PIPELINE ROBOT WITH EXISTING ROBOTS

Robot	Pip-diameter (mm)	Velocity (cm/s)	Mass (kg)	Size (mm)	Waterproof
Kako[11]	101-127	8.0	2.37	51 × 51×51	×
Yin[15]	129-160	12.70	2.5	25×12×12.4	×
Li[17]	90-110	0.43	1.56	80×5×5	×
Liu[18]	200-500	1.37	-	122×8.4×8.4	×
Li[22]	250-450	29.0	17.5	31×18.2×18	×
Ours	**100-400**	**50.0**	**1.0**	238×ϕ85	✓

V. CONCLUSIONS

To enhance the waterproofing, motion speed, and turning capability of pipeline robots, this study proposes a novel configuration scheme for a pipeline robot that can operate reliably in complex pipeline environments while maintaining strong water resistance. A multi-objective optimization framework was established to jointly optimize hydrodynamic performance, motion stability, and internal spatial layout, ensuring a low-drag external form while accommodating the integration of various onboard sensors. Using a task-driven design approach and sequential quadratic programming, the thruster arrangement was optimized to enable effective turning maneuvers within water-filled pipelines. Based on the optimization results, a dual-sphere robot prototype was developed, followed by hydrodynamic simulations and analyses. A series of experiments were then conducted: water tank tests demonstrated good maneuverability, while curved-pipe and T-junction tests verified the robot's passability and adaptability. Field trials in actual water supply pipelines further confirmed its flexibility and environmental adaptability. Currently, the robot uses direct propeller drive and can only move horizontally. Future work will focus on enabling multi-DOF motions (e.g., depth holding and climbing), enhancing cross-pipeline adaptability through rigid-flexible coupled mechanisms and control strategies, and developing autonomous navigation and inspection functions for practical engineering applications.

REFERENCES

[1] Jia Zhang, Mingnan Sun, Lin Qin, Dong Lin, Chang Liu, Jing Li, Chaolang Li, Shaomu Wen, Chuanjun Han, "In-line inspection methods and tools for oil and gas pipeline: A review, International Journal of Pressure Vessels and Piping," vol.214, pp.105409, 2025.

[2] Zefeng Yan,Qiuxia Fan,Qianqian Zhang,Lei Xu. Numerical and experimental investigation of bionic fairing for hydrodynamic performance optimization in amphibious unmanned platforms. Ocean Engineering, 349, 124049, 2026.

[3] Zefeng Yan, Mingda Li, Zihao Du, Xin Yang, Ying Luo, Xuedong Chen, Bin Han. Study on a tracked amphibious robot bionic fairing for drag reduction. Ocean Engineering, 267, 113223, 2023.

[4] Denan Xu, Zefeng Yan, Hengpeng Xie, Liang Lu, Ziyu Xiao, Bin Han. Demand-driven optimization method for thruster configuration of underwater vehicles considering capability boundary and system efficiency. Ocean Engineering, 310, 118749, 2024.

[5] Houjia Xu, Yuntao Li, Taotao Zhou, Fengyi Lan, Laibin Zhang, "An overview of the oil and gas pipeline safety in China," Journal of Industrial Safety, Vol.1, no.1, pp.100003, 2024.

[6] S. Kazeminasab, N. Sadeghi, V. Janfaza, M. Razavi, S. Ziyadidegan and M. K. Banks, "Localization, Mapping, Navigation, and Inspection Methods in In-Pipe Robots: A Review," in IEEE Access, vol. 9, pp. 162035-162058, 2021.

[7] Chaojie Xu, Wenming Jiang, Hongzhang Ma, Yang Liu, Huiyun Men, Xining Xu, Zhixin Li, "A Review: Research and Application of Pipeline Robots in the Oil and Gas Industry," Journal of Pipeline Science and Engineering, pp.2667-1433, pp.100356, 2025.

[8] J. M. M. Tur and W. Garthwaite, "Robotic devices for water main in pipe inspection: A survey," J. Field Robot., vol. 4, no. 27, pp. 491-508, 2010.

[9] Z. Hu and E. Appleton, "Dynamic characteristics of a novel self-drive pipeline pig," IEEE T rans . Robot., vol. 21, no. 5, pp. 781-789, 2005.

[10] Y. Oka, A. Kakogawa and S. Ma, "A Wheeled V-shaped In-Pipe Robot with Clutched Underactuated Joints," 2021 IEEE International Conference on Robotics and Automation (ICRA), Xi'an, China, pp. 11457-11462, 2021.

[11] A. Kakogawa, K. Murata and S. Ma, "Automatic T-Branch Travel of an Articulated Wheeled In-Pipe Inspection Robot Using Joint Angle Response to Environmental Changes," in IEEE Transactions on Industrial Electronics, vol. 70, no. 7, pp. 7041-7050, July 2023.

[12] C. J. Kaufman, Rocky Mountain Research Lab., Boulder, CO, private communication, May 1995.

[13] Y. -S. Kwon and B. -J. Yi, "Design and Motion Planning of a Two-Module Collaborative Indoor Pipeline Inspection Robot," in IEEE Transactions on Robotics, vol. 28, no. 3, pp. 681-696, June 2012.

[14] T. Zheng, P. Yuan, S. Feng, Y. Tian, H. Li and Q. Huang, "Key parameter design of wall pressing tracked pipeline robot under multiple constraint conditions," 2024 International Conference on Intelligent Robotics and Automatic Control (IRAC), Guangzhou, China, 2024, pp. 214-220.

[15] Jihua Yin, Xuemei Liu, Maokun Rui, Miao Yu, "Design and motion analysis of a simple screw driven in-pipe inspection robot base on adaptive variable pitch, Robotics and Autonomous Systems," vol. 1945, pp.105148, 2025.

[16] M. Wang, B. Bian, L. Cai, K. Li, Y. Pan and J. Chen, "Design of a Spiral Wheeled Adaptive Pipeline Robot," 2023 5th International Symposium on Robotics & Intelligent Manufacturing Technology (ISRIMT), Changzhou, China, pp. 15-20, 2023.

[17] Manhong Li, Guoliang Wang, Jingtian Wang, Yueshuo Zheng, Xin Jiao, "Development of an inchworm-like soft pipe robot for detection," International Journal of Mechanical Sciences, vol.253, pp. 108392, 2023.

[18] Jingwei Liu, Man Li, Yahui Wang, Da Zhao, Rui Deng, "Multi-gait snake robot for inspecting inner wall of a pipeline," Biomimetic Intelligence and Robotics, vol.4, no. 2, pp.100156, 2024.

[19] Ou Xie, Chenbo Zhang, Can Shen, Yufan Li, Dawei Zhou, "Study on the hydrodynamic performance of a self-propelled robot fish swimming in pipelines environment," Ocean Engineering, vol. 309, pp. 118356, 2024.

[20] Akira Oyama, Hirotaka Iida, Yonghoon Ji, Kazunori Umeda, Yuki Mano, Takumi Yasui, Taro Nakamura, "Three-dimensional Mapping of Pipeline from Inside Images Using Earthworm Robot Equipped with Camera," IFAC-PapersOnLine, vol.52, no.22, pp.87-90, 2019.

[21] M. Gao, M. Huang, K. Tang, X. Lang and J. Gao, "Design, Analysis, and Control of a Multilink Magnetic Wheeled Pipeline Robot," in IEEE Access, vol. 10, pp. 67168-67180, 2022.

[22] Q. Li and W. Zhao, "Design of a Modular Pipeline Robot Structure and Passing Ability Analysis," in IEEE Access, vol. 11, pp. 97978-97989, 2023.

[23] Liang Lu, Chengyuan Liang, Zefeng Yan, Hao Wang, Ming Xiang, Bin Han. Study on a foldable fairing for drag reduction of planetary wheelset. Ocean Engineering, 318, 120133,2025.